iScience

CellPress
OPEN ACCESS

Article

Automated 3D cytoplasm segmentation in soft X-ray tomography

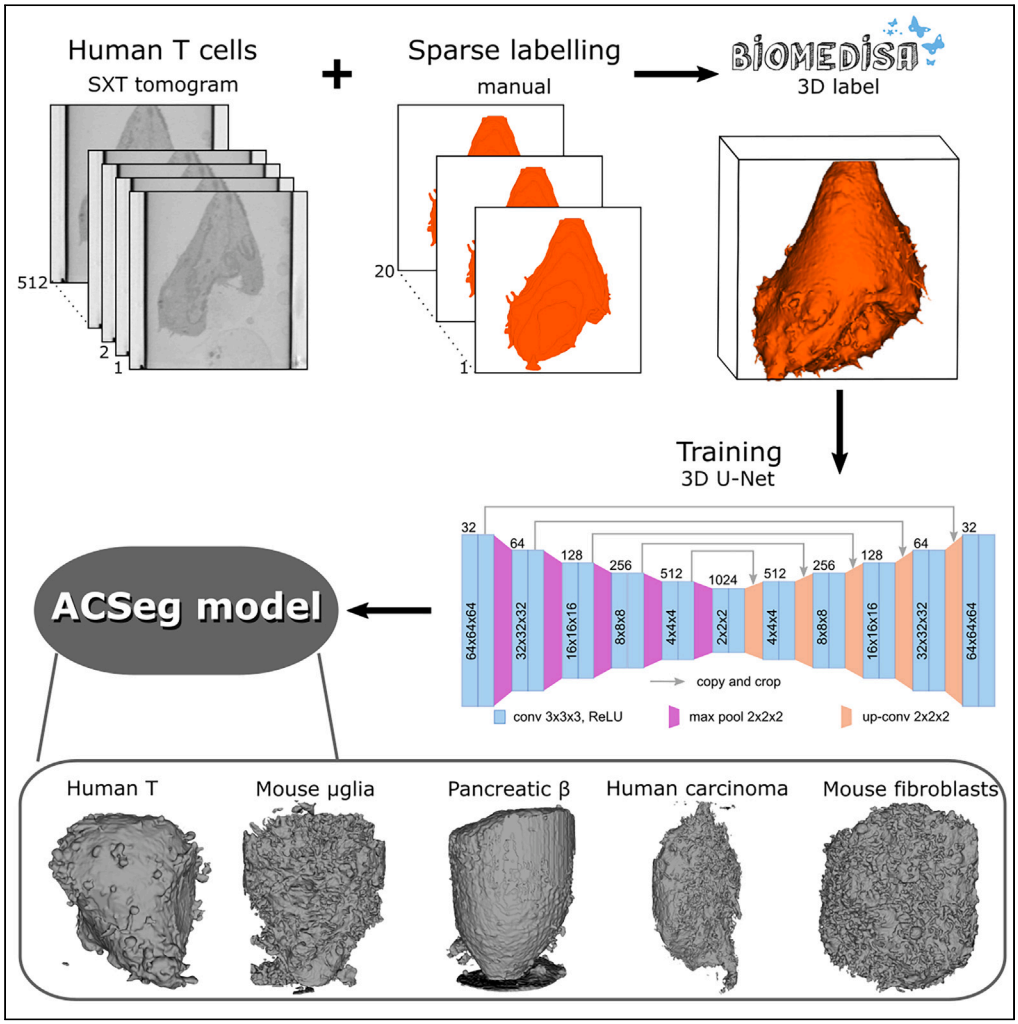

Ayse Erozan, Philipp D. Lösel, Vincent Heuveline, Venera Weinhardt

ayse.erozan@uni-heidelberg.de (A.E.)
venera.weinhardt@cos.uni-heidelberg.de (V.W.)

Highlights

Introducing ACSeg: an easy, plug-and-play model for cell cytoplasm extraction

ACSeg shows over 95% Dice score with only 20 datasets

ACSeg demonstrates generalization across 5 diverse cell types

To ease infection analysis, our model offers automatic cell cytoplasm segmentation

Erozan et al., iScience 27, 109856
June 21, 2024
https://doi.org/10.1016/j.isci.2024.109856

iScience

CellPress
OPEN ACCESS

Article

Automated 3D cytoplasm segmentation in soft X-ray tomography

Ayse Erozan,[1,2,3,*] Philipp D. Lösel,[2,3,4] Vincent Heuveline,[2,3] and Venera Weinhardt[1,5,6,*]

SUMMARY

Cells' structure is key to understanding cellular function, diagnostics, and therapy development. Soft X-ray tomography (SXT) is a unique tool to image cellular structure without fixation or labeling at high spatial resolution and throughput. Fast acquisition times increase demand for accelerated image analysis, like segmentation. Currently, segmenting cellular structures is done manually and is a major bottleneck in the SXT data analysis. This paper introduces ACSeg, an automated 3D cytoplasm segmentation model. ACSeg is generated using semi-automated labels and 3D U-Net and is trained on 43 SXT tomograms of immune T cells, rapidly converging to high-accuracy segmentation, therefore reducing time and labor. Furthermore, adding only 6 SXT tomograms of other cell types diversifies the model, showing potential for optimal experimental design. ACSeg successfully segmented unseen tomograms and is published on Biomedisa, enabling high-throughput analysis of cell volume and structure of cytoplasm in diverse cell types.

INTRODUCTION

The analysis of structure is a fundamental task in cell biology, as the size, shape, and internal anatomy of cells alter to enable new functions and adapt to changing environments, including pathological conditions.[1,2] Various disorders such as cancer, malaria, anemia,[1] and sickle cell disease[3] result in abnormal cell shape. With this in mind, determining the three-dimensional shape of cells is one of the most important aspects of cell biology.[4]

Thus, many microscopy techniques have been focused on imaging and analysis of the cell structure.[5–7] Among existing imaging techniques, soft X-ray tomography (SXT) enables imaging of whole mammalian cells with a spatial resolution of a few tens of nanometers, without labeling or chemical fixation, and at high throughput of 5 min for whole 3D volume.[8] While segmentation pipelines for light and electron microscopy are firmly established, automatic analysis of SXT data is limited.[9]

Most of the SXT-based structural cell analysis is based on manual segmentation.[8,10–12] Thresholding-based segmentation methods which require no prior labeled data have been proposed to extract mitochondria and cytoplasmic vesicles in the study by Nahas et al.[13,14] Cossa et al.[15] applied random forest segmentation to extract nucleoids from *Escherichia coli*. To extract mitochondria, Polo et al.[16] implemented a trainable Weka segmentation machine learning tool,[17] accessible in Fiji. Furthermore, neural network-based algorithms, such as convolutional neural networks or U-Net, have been used to extract membranous organelles in the study by Dyhr et al.,[9] Francis et al.,[18] and Egebjerg et al.[19] A segmentation method based on the combination of 2D U-Nets was used to automatically segment whole β-cells anatomy.[20] Most of these methods are designed for a very specialized organelle type or pathological condition, and automatic segmentation of whole-cell anatomy requires complex pre- and post-processing steps.

Here, we propose an easy plug-and-play model (ACSeg) based on 3D U-Net to extract the cell cytoplasm structure in various cell types. We exploit the semi-automatic segmentation based on 3D random walk implemented in the open platform Biomedisa.[21] Apart from minimizing the time for manual segmentation,[22] our results show that the high quality of segmented labels enables us to train the 3D U-Net on only 20 tomograms to achieve a Dice coefficient of 95.43%. Moreover, even though ACSeg was trained exclusively on tomograms containing human T cells, ACSeg was able to segment the cell cytoplasm of 4 unseen cell types with a Dice coefficient of about 87.62%. This accuracy could be significantly improved with only an additional 6 tomograms, diversifying ACSeg for automatic segmentation of various cell types. Interestingly, our data show that the success of ACSeg diversification depends on the type of cells and/or data quality, suggesting that optimal experimental design should be in focus for the training of 3D U-Nets. Considering the worldwide availability of SXT stations at the synchrotron sources[7] and an increase in the development of table-top instruments,[23] the application of SXT to the understanding of human diseases and development of novel drugs at the cellular level will continue to increase. Providing fast and accurate cell cytoplasm segmentation of

[1]Centre for Organismal Studies, Heidelberg University, Heidelberg, Germany
[2]Engineering Mathematics and Computing Lab, Interdisciplinary Center for Scientific Computing, Heidelberg University, Heidelberg, Germany
[3]Data Mining and Uncertainty Quantification, Heidelberg Institute for Theoretical Studies, Heidelberg, Germany
[4]Department of Materials Physics Research School of Physics, The Australian National University, Acton ACT, Australia
[5]Molecular Biophysics and Integrated Bioimaging Division, Lawrence Berkeley National Laboratory, Berkeley, CA, USA
[6]Lead contact
*Correspondence: ayse.erozan@uni-heidelberg.de (A.E.), venera.weinhardt@cos.uni-heidelberg.de (V.W.)
https://doi.org/10.1016/j.isci.2024.109856

Table 1. The effect of alteration of the number of tomograms for training on the Dice coefficient (%) of the model

No. of cells for training	Biomedisa labels	Manual labels
5	90.03 ± 15.61	86.81 ± 30.90
10	94.22 ± 15.33	87.69 ± 17.48
20	95.43 ± 11.94	90.93 ± 12.72
30	96.17 ± 11.00	92.61 ± 10.37
43	97.78 ± 2.13	93.87 ± 7.37

diverse cells imaged with SXT, ACSeg responds to the upcoming needs in automatic analysis of cell structure, which will be expanded to automatic segmentation of all cellular structures.

RESULTS

Automatic segmentation workflow for cell cytoplasm

To train our U-Net model for cytoplasm segmentation in SXT data, it is first necessary to generate 3D labels. To reduce manual work, we used Biomedisa for semi-automatic 3D segmentation.[22] We manually labeled every 20th slice in tomograms and submitted labels to Biomedisa for generating 3D labels by using smart interpolation, see Table 1. By use of semi-automatic labeling, we reduced the amount of manual work required to train the model by 94.6% compared to fully manual segmentation. The generated 3D labels along with 3D tomograms were used to train our U-Net model, implemented within Biomedisa for the automatic segmentation of cell cytoplasm. The segmentation workflow is summarized in Figure 1, where the trained network is depicted as ACSeg for the automatic cytoplasm segmentation.

Evaluation of ACSeg

Previous work on U-Net segmentation showed that the number and quality of training datasets are crucial to achieving high accuracy of segmentation.[24,25] Therefore, we have measured the accuracy of the ACSeg by computing Dice coefficients[26,27] for U-Net trained on various SXT tomograms. We trained the ACSeg on 5, 10, 20, 30, and 43 datasets, see Figure 2. With only 20 training datasets, our ACSeg achieved a Dice coefficient above 95%. We have investigated whether such fast convergence of Dice coefficient is due to the higher quality of semi-automatic segmentation in the prediction of labels which was mentioned in insect studies.[25] We have compared the ACSeg trained on manually segmented labels in comparison to semi-automatically with Biomedisa. The ACSeg trained on the manual labels showed a lower Dice coefficient for 5 training datasets with 87% accuracy compared to 90% with ACSeg trained on 3D labels from Biomedisa, see Figure 2. Interestingly, this relatively low difference of 3% in accuracy is not compensated by the increased number of tomograms. ACSeg trained on 43 datasets resulted in 94% for manually labeled data and 98% for Biomedisa-labeled data. We have fitted the so-called 1st order delay function, that is $1-b\cdot\exp(-ax)$, to find the number of manually labeled tomograms required to achieve 98% accuracy. This approximation shows that about 52 additional manually segmented tomograms (95 in total) would be required to achieve the same accuracy as ACSeg trained on 43 semi-automatically segmented datasets.

For ACSeg trained on Biomedisa results, adding 10 datasets increases the accuracy at first steeply but then only gradually with more than 20 datasets, suggesting that the addition of more datasets is unnecessary. It has been shown that choosing the Dice coefficient as a performance metric is often not an adequate measure for training models.[27] To assess the performance of the ACSeg from the biological perspective, we calculated two major parameters used in cell biology to normalize for cell variability and change of structure, that is volume and surface-to-volume ratio of cells.[10] We found no significant difference in volume (Figure 3A) compared between ground truth (generated with Biomedisa) by producing Biomedisa and ACSeg predictions. On the contrary, the probability for the surface-to-volume ratio is only 0.001478 (Figure 3B). Consistent with this, we found differences in the cytoplasmic morphology that are noticeable in 3D renderings (Figures $3C_3$ and $3C_4$). Many cells have cytoplasmic projections with fine ultrastructure which is hard to detect automatically. Noticeably, the ACSeg segmentation did not predict the ultrastructure of some filopodia in comparison to the ground truth. We have considered that the reason behind the low surface-to-volume ratio is that there is a considerable loss in surface resolution due to dataset scaling. Therefore, similar to the electron microscopy approach of local regional segmentation,[28] we have trained a second-level ACSeg model which would work on the volumes of interest of 64 × 64 × 64 voxels along the cell surface. While this second-level refinement of filopodia should increase in Dice score by 1% compared to ACSeg, the surface area to volume ratio measurements were still significantly different in comparison to the ground truth. To compensate for the lack of precision in cell topology segmentation, the ACSeg model could be potentially combined with other approaches, for example, conditional random fields, graph search, and active contour.[29–31]

In conclusion, the ACSeg trained on 43 datasets is sufficient to successfully predict the gross cell volume and most of the filopodia, which are sufficient for morphological analysis where cell volume is used for normalization and visual structural representation used in cell biology.

Comparison of ACSeg to other approaches

Intuitively, one could think that cytoplasm segmentations in the SXT data should be easy to capture by conventional approaches, such as thresholding. It is worth mentioning that the content of SXT tomograms varies a lot. For SXT imaging, cells are suspended in thin-wall glass

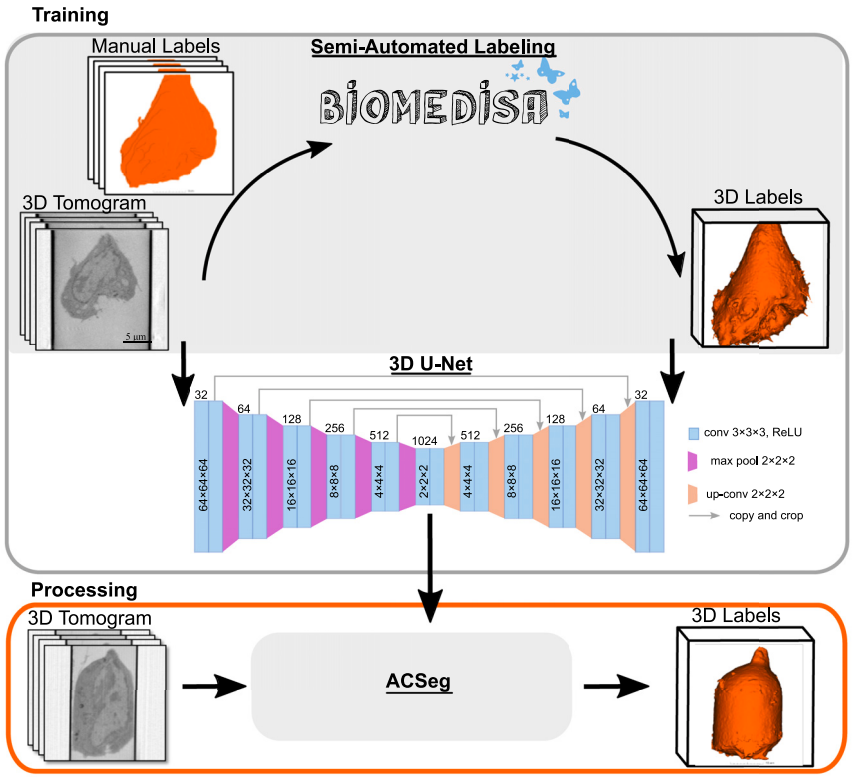

Figure 1. Automated cytoplasm segmentation workflow with semi-automated labeling

capillary inside the microscope.[32] Many cells are touching the capillary wall. Additionally, polystyrene beads are added for SXT normalization in the imaging of large cells. Their distribution is random and not consistent between tomograms. The biology of cells starts to play a role as well. Some cells are apoptotic with fragments of their cytoplasm visible in SXT tomograms. All these effects are stochastic and cannot be controlled in the SXT experiments. To demonstrate this effect, we show 4 cases in Figure 4: an isolated cell with debris from other cells, a cell touching the glass capillary, cells tightly packed in the capillary, and a cell between two polystyrene beads. We have used thresholding methods, such as the adaptive and Otsu thresholding, which do not perform well in segmentation in most cases, see Figure 4. While these methods can be optimized with pre- and post-processing to increase segmentation quality, such an optimization pipeline would need to be adjusted to individual cases. The ACSeg segmentation of these difficult cases remains accurate without any pre- and post-processing steps.

With the increase of AI-based models for automatic segmentation of images from different microscopy techniques,[28,33] we compared ACSeg to the increasingly used Segment Anything Model (SAM) developed by Meta AI.[34] As for classical approaches, we selected the same different scenarios of the cells imaged with SXT, see Figure 5.[34] As SAM is trained on 2D datasets, we have applied the models to the central virtual slices of the 3D tomogram. Among four scenarios, the SAM model could identify individual cells in all except where multiple cells were touching each other. In this case, the cell nucleus was found as a distinct and dominant feature. Though in other scenarios the cells have been identified successfully, fine details such as cell filopodia were not fully captured. That is reflected in the lower Dice score coefficient of 97.53% for SAM versus 99.57% for ACSeg as calculated for 2D slices. Applying SAM on other slices to segment 3D cell cytoplasm would require modification of the model.[35–37] This adaption, however, is impractical as ACSeg requires such a minimal number of datasets and shows a high accuracy of 95% for cytoplasm segmentation. Even compared to existing models trained on SXT datasets of pancreatic beta cells,[20] the ACSeg model achieved the Dice score of 94.31% in comparison to 91.60%, even though it was not trained on this specific cell type.

ACSeg transfer to other cell types

Because the cells are so diverse in size and morphology, it is typically difficult to apply a segmentation network trained on one type of cells to others. We therefore first tested our model on the open SXT datasets of β-cells (INS-1E – a rat insulinoma cell line). Li et al. already segmented cytoplasm and some organelles.[20] Comparing cytoplasm segmentation, we achieved 95.31% ± 5.59% Dice coefficient for 3 tomograms which is slightly better than the results from Li's study (dice coefficient of 91.60% ± 2.19%).

To test even more divergent cell types, we have tested ACSeg on SXT datasets of hepatocyte-derived carcinoma Huh-7, murine microglia BV-2, and mouse embryonic fibroblast (MEF) cells, see Table 2. For MEF cells, the ACSeg showed high accuracy with 94.43% measured by the Dice coefficient. The segmentation of Huh-7 and BV-2 cells, however, was not successful with 82.93% and 84.06% Dice coefficients, respectively. To

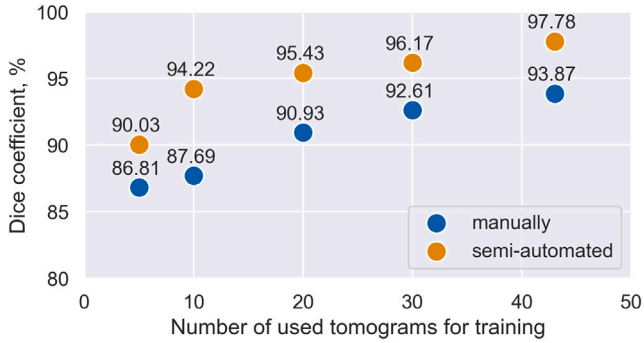

Figure 2. Dice coefficient according to alteration of the number of the training data

see whether ACSeg will have higher accuracy by generalization of training datasets, we included other cell types. We have added to 43 3D labels of T cells, 3D labels of 6 SXT tomograms for Huh-7 cells to our training data. Interestingly with the addition of such a small number of data, the re-trained ACSeg showed a 10% increase not only for Huh-7 cells but also for BV-2 cells. We explored whether ACSeg can be successfully generalized by using an equivalent number of training datasets from BV-2 cells. The ACSeg trained on 43 3D labels of T cells and 6 BV-2 cells showed lower accuracy than generalization with Huh-7 cells with Dice coefficients of 90.25%, 87.67%, and 94.58% for BV-2, Huh-7, and MEF cells correspondingly. Similarly, we generalized ACSeg by the addition of 6 MEF cells and a mixture of Huh-7, BV-2, and MEF cells (6 tomograms each). Although both retraining processes provided to increase in the overall Dice coefficient, they, however, have not reached the success obtained from the network trained by combining 43 T cells with 6 Huh-7. The experiments revealed that the best accuracy measured by the Dice coefficient was ACSeg trained on 43 T cells and 6 Huh-7 cells. Based on 3D labels segmented by ACSeg and Biomedisa (Figure 6), we can say that Huh-7 cells are more similar in number and structure of filopodia to BV-2 than T cells. However, at the moment, we have no explanation why the generalization of the ACSeg on BV-2 cells does not increase accuracy on the same scale for Huh-7 cells, and why the same accuracy is achieved for MEF cells independent of AC-Seg generalization.. Possible metrics affecting the generalization of the ACSeg are under investigation.

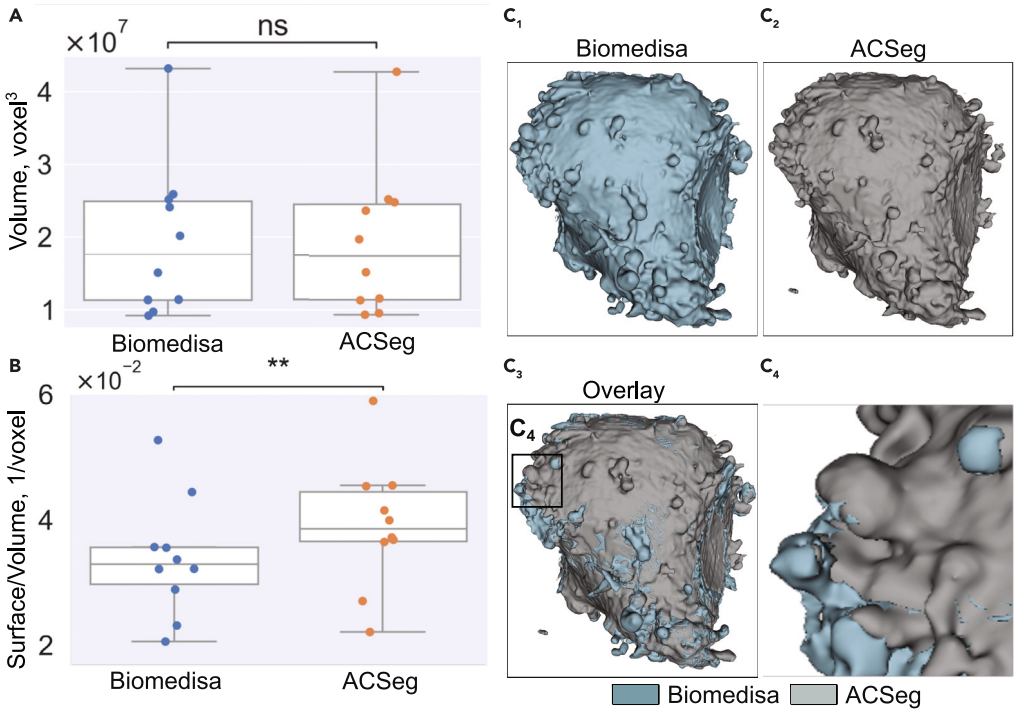

Figure 3. ACSeg segmentation and morphological quantification of T cells

The volume (A) and surface area to volume ratio (B) of the cell were measured in the ground truth and prediction of cytoplasm segmentation with the ACSeg. *ns* : $p > 0.05$, *: $0.01 < p <= 0.05$, **: $0.001 < p <= 0.01$, using paired t test. $N = 10$.

(C) 3D rendering of Biomedisa (C1) and prediction of the ACSeg (C2), respectively, visual comparison of Biomedisa and our model's prediction (C3). The box in C3 denotes the area shown up closely in C4.

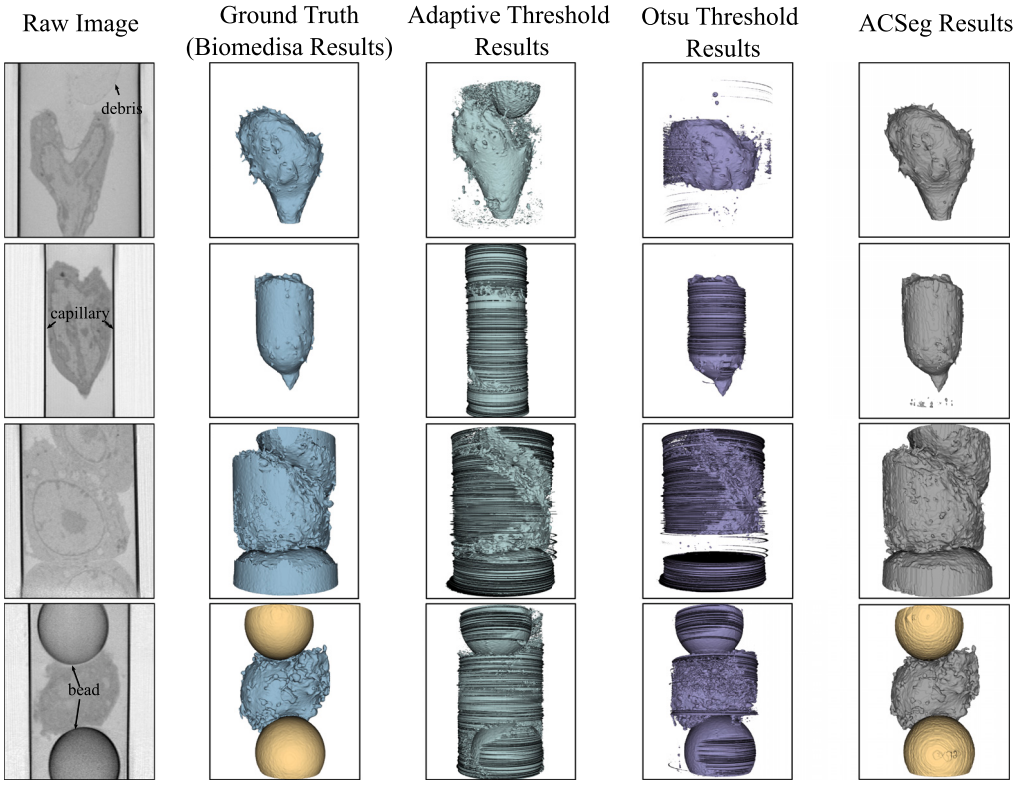

Figure 4. 3D quantification of cytoplasm segmentation accuracy for classical approaches

DISCUSSION

Our work presents a pipeline for training a 3D U-Net on semi-automatically segmented SXT datasets for robust automatic segmentation of the cellular cytoplasm (ACSeg). Since machine learning and deep learning algorithms rely heavily on accurately labeled data that require expert knowledge, extensive time, and effort to train, we investigated a semi-automated segmentation approach using Biomedisa to generate increased quality of labeled training data for a 3D U-Net, generating a model that can segment the cytoplasm with high accuracy of more than 95% within 1 min. The use of labels generated with Biomedisa provides faster convergence in training to higher Dice coefficient compared to manual segmentation. These results illustrate that the quality of the labeling in the training dataset for the 3D cytoplasm segmentation is an important factor in achieving a decent Dice coefficient with less training data.

Even though we achieved a high Dice coefficient with our model, we did not rely only on this pixel-wise metric. In biology, segmented images are mostly used for statistical analysis of cell morphology. For this reason, we compared volume and surface-to-volume ratio as evaluation metrics as well. While the cell volume obtained with ACSeg is accurately measured, the surface-to-volume ratio of cells is not accurate. We believe this is due to build in scaling of tomograms to a size of 256 × 256 × 256 voxels. To achieve higher accuracy for fine features of the cell cytoplasm, alternative architectures such as Double U-Net should be considered.[38] Such an approach will help to improve the segmentation of fine features without a drastic increase in time for model training.

Although our model was trained on tomograms containing only one cell type, we have applied it to other cells of distinct morphology. Without any pre-processing methods, ACSeg showed a high accuracy of more than 95% for β-cells and MEF cells.[20] For cells with lower accuracy, such as mouse microglia (BV-2) and hepatocyte-derived carcinoma cells (Huh-7) cells, we generalize ACSeg with the addition of a very small number of datasets in the training. Interestingly, the results show that there is cell type (or dataset)-specific success of model generalization. We expect that identifying optimal experimental design in terms of image quality and cell type should enable the development of automatic segmentation models based on a small number of datasets.

Limitations of the study

In this paper, we described an automatic segmentation method based on a 3D U-Net and a semi-automated labeling tool—Biomedisa—to automatically segment the cytoplasm of cells in SXT data with our ACSeg model. While ACSeg shows promising results, it is important to acknowledge certain limitations. One notable consideration is the diverse nature of data collection methods. While our model applies to SXT imaging of cells in capillaries, other SXT facilities utilize flat specimen holders, such as transmission electron microscopy grids. This variation in data collection approaches leads to differences in image characteristics, potentially affecting ACSeg's performance.

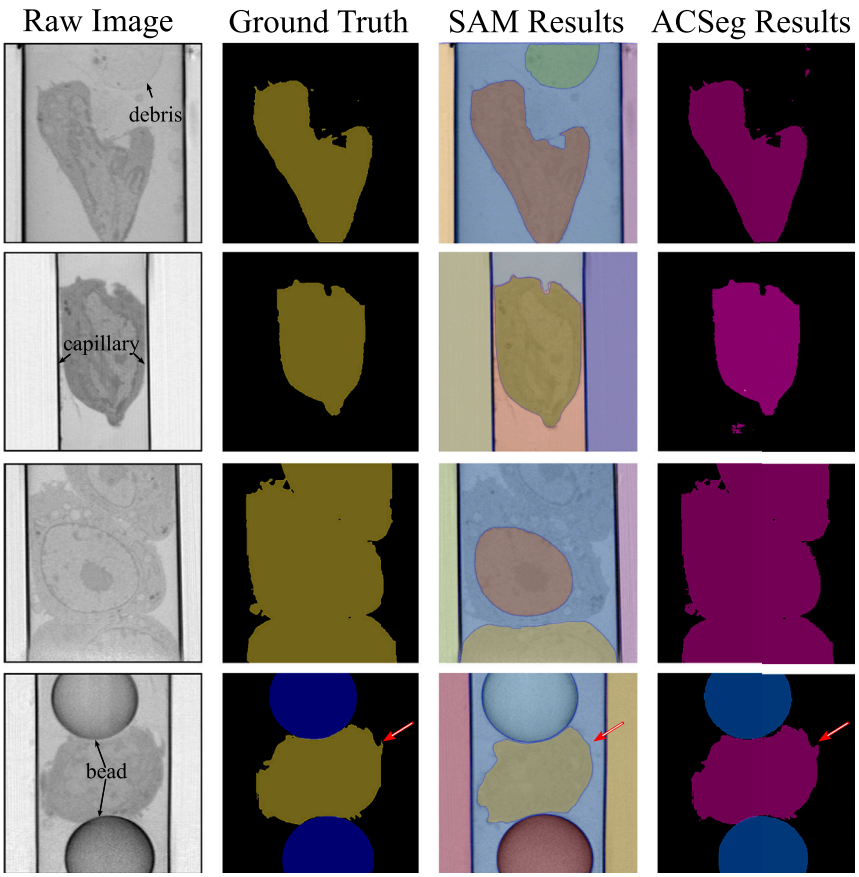

Figure 5. 2D quantification of cytoplasm segmentation accuracy in comparison to SAM

STAR★METHODS

Detailed methods are provided in the online version of this paper and include the following:

- KEY RESOURCES TABLE
- RESOURCE AVAILABILITY
  - Lead contact
  - Materials availability
  - Data and code availability
- EXPERIMENTAL MODEL AND STUDY PARTICIPANT DETAILS
  - Soft-X-ray tomography
  - Dataset
- METHOD DETAILS
  - Semi-automated labeling
  - Model training
- QUANTIFICATION AND STATISTICAL ANALYSIS

Table 2. Dice coefficient results of ACSeg and its variants on divergent cell types

# of tomograms for training	BV-2 (12)	Huh-7 (12)	MEF (9)
43 (T)	83.19 ± 30.52	85.01 ± 23.98	94.43 ± 7.04
43 (T) + 6 (BV-2)	90.25 ± 13.90	87.67 ± 27.89	94.58 ± 6.21
43 (T) + 6 (Huh-7)	95.49 ± 1.57	94.90 ± 10.95	94.56 ± 7.45
43 (T) + 6 (MEF)	88.95 ± 17.72	86.76 ± 24.51	94.80 ± 7.07
43 (T) + 6 (Huh-7) + 6 (BV-2) + 6 (MEF)	92.82 ± 12.70	90.61 ± 31.29	94.74 ± 6.73

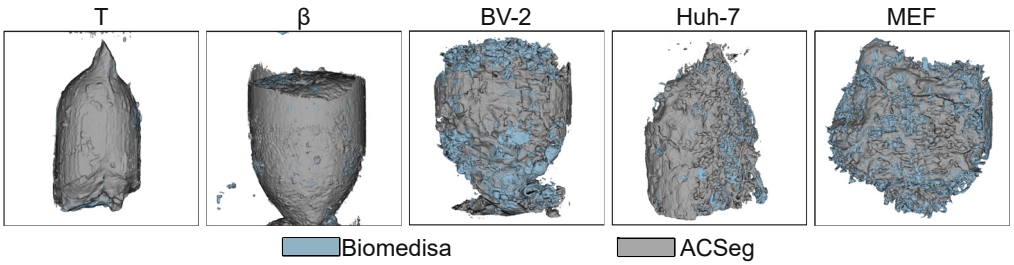

Figure 6. Prediction of the ACSeg over T, BV-2, Huh-7, and MEF cells

ACKNOWLEDGMENTS

The work was funded within the framework of the Excellence Strategy of the Federal and State Governments of Germany and by the CoCID project (no. 101017116) funded within EU Research and Innovation Act. We thank Anthoula Chatzimpinou (COS, Heidelberg University), Maija Vihinen-Ranta (University of Jyväskylä, Finland), and Kate White (University of Southern California, USA) for providing the datasets. We are grateful to Axel Ekman, AG Wittbrodt (COS, Heidelberg University), Alexander Zeilmann, and Carolyn Larabell for their fruitful discussions and feedback on this research. For the publication fee, we acknowledge financial support by Heidelberg University.

AUTHOR CONTRIBUTIONS

A.E. performed the experiments and formal analysis. A.E. and P.D.L. provided methodology and software. V.W. and V.H. provided expertise and feedback. V.W. conceived the experiments, provided samples, and secured funding. A.E. and V.W. wrote the manuscript, and P.D.L. and V.H. conducted the review and editing.

DECLARATION OF INTERESTS

The authors declare no competing interests.

Received: December 19, 2023
Revised: March 22, 2024
Accepted: April 27, 2024
Published: April 29, 2024

REFERENCES

1. Weinhardt, V., Chen, J.H., Ekman, A., McDermott, G., Le Gros, M.A., and Larabell, C. (2019). Imaging cell morphology and physiology using X-rays. Biochem. Soc. Trans. *47*, 489–508. https://doi.org/10.1042/BST20180036.
2. Michael, J. (2021). What do we mean when we talk about "structure/function" relationships? Adv. Physiol. Educ. *45*, 880–885. https://doi.org/10.1152/advan.00108.2021.
3. Darrow, M.C., Zhang, Y., Cinquin, B.P., Smith, E.A., Boudreau, R., Rochat, R.H., Schmid, M.F., Xia, Y., Larabell, C.A., and Chiu, W. (2016). Visualizing red blood cell sickling and the effects of inhibition of sphingosine kinase 1 using soft X-ray tomography. J. Cell Sci. *129*, 3511–3517. https://doi.org/10.1242/jcs.189225.
4. Liu, P.Y., Chin, L.K., Ser, W., Chen, H.F., Hsieh, C.M., Lee, C.H., Sung, K.B., Ayi, T.C., Yap, P.H., Liedberg, B., et al. (2016). Cell refractive index for cell biology and disease diagnosis: past, present and future. Lab Chip *16*, 634–644. https://doi.org/10.1039/C5LC01445J.
5. Gurcan, M.N., Boucheron, L.E., Can, A., Madabhushi, A., Rajpoot, N.M., and Yener, B. (2009). Histopathological image analysis: A review. IEEE Rev. Biomed. Eng. *2*, 147–171. https://doi.org/10.1109/RBME.2009.2034865.
6. Gordon, R.E. (2014). Electron microscopy: a brief history and review of current clinical application. Methods Mol. Biol. *1180*, 119–135. https://doi.org/10.1007/978-1-4939-1050-2_7.
7. Harkiolaki, M., Darrow, M.C., Spink, M.C., Kosior, E., Dent, K., and Duke, E. (2018). Cryo-soft X-ray tomography: using soft X-rays to explore the ultrastructure of whole cells. Emerg. Top. Life Sci. *2*, 81–92. https://doi.org/10.1042/ETLS20170086.
8. Loconte, V., Chen, J.-H., Cortese, M., Ekman, A., Le Gros, M.A., Larabell, C., Bartenschlager, R., and Weinhardt, V. (2021). Using soft X-ray tomography for rapid whole-cell quantitative imaging of SARS-CoV-2-infected cells. Cell Rep. Methods *1*, 100117. https://doi.org/10.1016/j.crmeth.2021.100117.
9. Dyhr, M.C.A., Sadeghi, M., Moynova, R., Knappe, C., Kepsutlu Çakmak, B., Werner, S., Schneider, G., McNally, J., Noé, F., and Ewers, H. (2023). 3D surface reconstruction of cellular cryo-soft X-ray microscopy tomograms using semisupervised deep learning. Proc. Natl. Acad. Sci. USA *120*, e2209938120. https://doi.org/10.1073/pnas.2209938120.
10. Loconte, V., Singla, J., Li, A., Chen, J.H., Ekman, A., McDermott, G., Sali, A., Le Gros, M., White, K.L., and Larabell, C.A. (2022). Soft X-ray tomography to map and quantify organelle interactions at the mesoscale. Structure *30*, 510–521.e3. https://doi.org/10.1016/j.str.2022.01.006.
11. Loconte, V., Chen, J.-H., Vanslembrouck, B., Ekman, A.A., McDermott, G., Le Gros, M.A., and Larabell, C.A. (2023). Soft X-ray tomograms provide a structural basis for whole-cell modeling. Faseb. J. *37*, e22681. https://doi.org/10.1096/fj.202200253R.
12. Schneider, G., Guttmann, P., Heim, S., Rehbein, S., Mueller, F., Nagashima, K., Heymann, J.B., Müller, W.G., and McNally, J.G. (2010). Three-dimensional cellular ultrastructure resolved by X-ray microscopy. Nat. Methods *7*, 985–987. https://doi.org/10.1038/nmeth.1533.
13. Nahas, K., and Harkiolaki, M. (2022). Contour: A Semi-automated Segmentation and Quantitation Tool for Cryo-Soft-X-Ray Tomography (Cambridge University Press). https://doi.org/10.1017/S2633903X22000046.
14. Nahas, K.L., Connor, V., Scherer, K.M., Kaminski, C.F., Harkiolaki, M., Crump, C.M., and Graham, S.C. (2022). Near-native state imaging by cryo-soft-X-ray tomography

reveals remodelling of multiple cellular organelles during HSV-1 infection. PLoS Pathog. *18*, e1010629. https://doi.org/10.1371/journal.ppat.1010629.

15. Cossa, A., Trépout, S., Wien, F., Groen, J., Le Brun, E., Turbant, F., Besse, L., Pereiro, E., and Arluison, V. (2022). Cryo soft Xray tomography to explore Escherichia coli nucleoid remodeling by Hfq master regulator. J. Struct. Biol. *214*, 107912. https://doi.org/10.1016/j.jsb.2022.107912.
16. Polo, C.C., Fonseca-Alaniz, M.H., Chen, J.-H., Ekman, A., McDermott, G., Meneau, F., Krieger, J.E., and Miyakawa, A.A. (2020). Three-dimensional imaging of mitochondrial cristae complexity using cryo-soft X-ray tomography. Sci. Rep. *10*, 21045. https://doi.org/10.1038/s41598-020-78150-3.
17. Arganda-Carreras, I., Kaynig, V., Rueden, C., Eliceiri, K.W., Schindelin, J., Cardona, A., and Sebastian Seung, H. (2017). Trainable Weka Segmentation: a machine learning tool for microscopy pixel classification. Bioinformatics *33*, 2424–2426. https://doi.org/10.1093/bioinformatics/btx180.
18. Francis, J.P., Wang, H., White, K., Syeda-Mahmood, T., and Stevens, R. (2020). Neural network segmentation of cell ultrastructure using incomplete annotation. In 2020 IEEE 17th International Symposium on Biomedical Imaging (ISBI), pp. 1183–1187. https://doi.org/10.1109/ISBI45749.2020.9098739.
19. Egebjerg, J.M., Szomek, M., Thaysen, K., Juhl, A.D., Kozakijevic, S., Werner, S., Pratsch, C., Schneider, G., Kapishnikov, S., Ekman, A., et al. (2024). Automated quantification of vacuole fusion and lipophagy in Saccharomyces cerevisiae from fluorescence and cryo-soft X-ray microscopy data using deep learning. Autophagy *20*, 902–922. https://doi.org/10.1080/15548627.2023.2270378.
20. Li, A., Zhang, X., Singla, J., White, K., Loconte, V., Hu, C., Zhang, C., Li, S., Li, W., Francis, J.P., et al. (2022). Auto-segmentation and time-dependent systematic analysis of mesoscale cellular structure in **β**-cells during insulin secretion. PLoS One *17*, e0265567. https://doi.org/10.1371/journal.pone.0265567.
21. Lösel, P., and Heuveline, V. (2016). Enhancing a diffusion algorithm for 4D image segmentation using local information. In Medical Imaging 2016: Image Processing, *9784*Medical Imaging 2016: Image Processing (SPIE), pp. 707–717. https://doi.org/10.1117/12.2216202.
22. Lösel, P.D., van de Kamp, T., Jayme, A., Ershov, A., Faragó, T., Pichler, O., Tan Jerome, N., Aadepu, N., Bremer, S., Chilingaryan, S.A., et al. (2020). Introducing Biomedisa as an open-source online platform for biomedical image segmentation. Nat. Commun. *11*, 5577. https://doi.org/10.1038/s41467-020-19303-w.
23. Fahy, K., McEnroe, T., O'Reilly, F., Fyans, W., Skoko, D., and Sheridan, P. (2020). Development of a commercial laboratory scale soft x-ray microscope. Microsc. Microanal. *26*, 3008–3009. https://doi.org/10.1017/S1431927617005578.
24. Lösel, P.D., Monchanin, C., Lebrun, R., Jayme, A., Relle, J.J., Devaud, J.M., Heuveline, V., and Lihoreau, M. (2023). Natural variability in bee brain size and symmetry revealed by micro-CT imaging and deep learning. PLoS Comput. Biol. *19*, e1011529. https://doi.org/10.1371/journal.pcbi.1011529.
25. Nemoto, T., Futakami, N., Kunieda, E., Yagi, M., Takeda, A., Akiba, T., Mutu, E., and Shigematsu, N. (2021). Effects of sample size and data augmentation on U-Net-based automatic segmentation of various organs. Radiol. Phys. Technol. *14*, 318–327. https://doi.org/10.1007/s12194-021-00630-6.
26. Maier-Hein, L., Eisenmann, M., Reinke, A., Onogur, S., Stankovic, M., Scholz, P., Arbel, T., Bogunovic, H., Bradley, A.P., Carass, A., et al. (2018). Why rankings of biomedical image analysis competitions should be interpreted with care. Nat. Commun. *9*, 5217. https://doi.org/10.1038/s41467-018-07619-7.
27. Maier-Hein, L., Reinke, A., Godau, P., Tizabi, M.D., Buettner, F., Christodoulou, E., Glocker, B., Isensee, F., Kleesiek, J., Kozubek, M., et al. (2024). Metrics reloaded: recommendations for image analysis validation. Nat. Methods *21*, 195–212. https://doi.org/10.1038/s41592-023-02151-z.
28. Heinrich, L., Bennett, D., Ackerman, D., Park, W., Bogovic, J., Eckstein, N., Petruncio, A., Clements, J., Pang, S., Xu, C.S., et al. (2021). Whole-cell organelle segmentation in volume electron microscopy. Nature *599*, 141–146. https://doi.org/10.1038/s41586-021-03977-3.
29. Zhou, L., Zhong, Z., Shah, A., Qiu, B., Buatti, J., and Wu, X. (2019). Deep neural networks for surface segmentation meet conditional random fields. Preprint at arXiv. https://doi.org/10.48550/arXiv.1906.04714.
30. Yin, Y., Zhang, X., Williams, R., Wu, X., Anderson, D.D., and Sonka, M. (2010). LOGISMOS—layered optimal graph image segmentation of multiple objects and surfaces: cartilage segmentation in the knee joint. IEEE Trans. Med. Imag. *29*, 2023–2037. https://doi.org/10.1109/TMI.2010.2058861.
31. Hemalatha, R., Thamizhvani, T., Dhivya, A.J.A., Joseph, J.E., Babu, B., and Chandrasekaran, R. (2018). Active contour based segmentation techniques for medical image analysis. Med. Biol. Image Anal. *4*, 2. https://doi.org/10.5772/intechopen.74576.
32. Chen, J.H., Vanslembrouck, B., Loconte, V., Ekman, A., Cortese, M., Bartenschlager, R., McDermott, G., Larabell, C.A., Le Gros, M.A., and Weinhardt, V. (2022). A protocol for full-rotation soft X-ray tomography of single cells. STAR Protoc. *3*, 101176. https://doi.org/10.1016/j.xpro.2022.101176.
33. Basu, A., Senapati, P., Deb, M., Rai, R., and Dhal, K.G. (2023). A survey on recent trends in deep learning for nucleus segmentation from histopathology images. Evol. Syst. 1–46. https://doi.org/10.1007/s12530-023-09491-3.
34. Kirillov, A., Mintun, E., Ravi, N., Mao, H., Rolland, C., Gustafson, L., Xiao, T., Whitehead, S., Berg, A.C., Lo, W.Y., et al. (2023). Segment anything. In Proceedings of the IEEE/CVF International Conference on Computer Vision, pp. 4015–4026.
35. Gallagher, J.E., Gogia, A., and Oughton, E.J. (2024). A Multispectral Automated Transfer Technique (MATT) for machine-driven image labeling utilizing the Segment Anything Model (SAM). Preprint at arXiv. https://doi.org/10.48550/arXiv.2402.11413.
36. Zhang, Y., and Jiao, R. (2023). How segment anything model (SAM) boost medical image segmentation?. Preprint at arXiv. https://doi.org/10.48550/arXiv.2305.03678.
37. Zhang, C., Liu, L., Cui, Y., Huang, G., Lin, W., Yang, Y., and Hu, Y. (2023). A comprehensive survey on segment anything model for vision and beyond. Preprint at arXiv. https://doi.org/10.48550/arXiv.2305.08196.
38. Smith, M.B., Sparks, H., Almagro, J., Chaigne, A., Behrens, A., Dunsby, C., and Salbreux, G. (2023). Active mesh and neural network pipeline for cell aggregate segmentation. Biophys. J. *122*, 1586–1599. https://doi.org/10.1016/j.bpj.2023.03.038.
39. Le Gros, M.A., McDermott, G., Cinquin, B.P., Smith, E.A., Do, M., Chao, W.L., Naulleau, P.P., and Larabell, C.A. (2014). Biological soft X-ray tomography on beamline 2.1 at the Advanced Light Source. J. Synchrotron Radiat. *21*, 1370–1377. https://doi.org/10.1107/S1600577514015033.
40. Weinhardt, V., Chen, J.H., Ekman, A.A., Guo, J., Remesh, S.G., Hammel, M., McDermott, G., Chao, W., Oh, S., Le Gros, M.A., and Larabell, C.A. (2020). Switchable resolution in soft x-ray tomography of single cells. PLoS One *15*, e0227601. https://doi.org/10.1371/journal.pone.0227601.
41. Parkinson, D.Y., Knoechel, C., Yang, C., Larabell, C.A., and Le Gros, M.A. (2012). Automatic alignment and reconstruction of images for soft X-ray tomography. J. Struct. Biol. *177*, 259–266. https://doi.org/10.1016/j.jsb.2011.11.027.
42. Fedorov, A., Beichel, R., Kalpathy-Cramer, J., Finet, J., Fillion-Robin, J.C., Pujol, S., Bauer, C., Jennings, D., Fennessy, F., Sonka, M., et al. (2012). 3D Slicer as an image computing platform for the Quantitative Imaging Network. Magn. Reson. Imag. *30*, 1323–1341. https://doi.org/10.1016/j.mri.2012.05.001.
43. Kikinis, R., Pieper, S.D., and Vosburgh, K.G. (2013). 3D Slicer: a platform for subject-specific image analysis, visualization, and clinical support. In Intraoperative imaging and image-guided therapy (Springer New York), pp. 277–289. https://doi.org/10.1007/978-1-4614-7657-3_19.
44. Çiçek, Ö., Abdulkadir, A., Lienkamp, S.S., Brox, T., and Ronneberger, O. (2016). 3D U-Net: learning dense volumetric segmentation from sparse annotation. In Medical Image Computing and Computer-Assisted Intervention–MICCAI 2016: 19th International Conference, Athens, Greece, October 17-21, 2016, Proceedings, Part II 19 (Springer International Publishing), pp. 424–432. https://doi.org/10.1007/978-3-319-46723-8_49.
45. Schindelin, J., Arganda-Carreras, I., Frise, E., Kaynig, V., Longair, M., Pietzsch, T., Preibisch, S., Rueden, C., Saalfeld, S., Schmid, B., et al. (2012). Fiji: an open-source platform for biological-image analysis. Nat. Methods *9*, 676–682. https://doi.org/10.1038/nmeth.2019.

STAR★METHODS

KEY RESOURCES TABLE

REAGENT or RESOURCE	SOURCE	IDENTIFIER
Deposited data		
T cells	heiData	https://doi.org/10.11588/data/XEBZLL
Software and algorithms		
Biomedisa	Lösel et al.[22]	https://biomedisa.info/
ImageJ – Fiji 1.54 f	Schindelin et al.[45]	https://imagej.net/ij/
Python version 3.9.7	Python Software Foundation	https://www.python.org/
Slicer 5.0.3	Fedorov et al.[42], Kikinis et al.[43]	https://www.slicer.org/
Other		
ACSeg model	This paper	https://biomedisa.info/gallery/

RESOURCE AVAILABILITY

Lead contact

Further information and requests for resources and reagents should be directed to and will be fulfilled by the lead contact, Venera Weinhardt (venera.weinhardt@cos.uni-heidelberg.de).

Materials availability

This study did not generate new reagents.

Data and code availability

- Data have been deposited at heiData are publicly available as of the date of publication and, ACSeg model has been published on the Biomedisa. The DOIs are listed in the key resources table.
- This paper does not report the original code.
- Any additional information required to reanalyze the data reported in this paper is available from the lead contact upon request.

EXPERIMENTAL MODEL AND STUDY PARTICIPANT DETAILS

Soft-X-ray tomography

SXT imaging was performed at the XM-2 beamline of the Advanced Light Source at the Lawrence Berkeley National Laboratory.[39] We have used a 60 nm outermost zone width Fresnel Zone plate to image cells in full rotation tomography.[40] The cells were mixed with polystyrene beads, and plunge-frozen in thin-wall glass capillaries and 92 x-ray projection images were acquired over 180° rotation with an exposure time of 200 ms. The 3D reconstructions of cells were obtained with AREC3D.[41] Further experimental details can be found elsewhere.[32]

Dataset

On average, the tomograms have dimensions of 472 × 472 × 491 voxels with slight variability due to shifting of the capillary in the x-ray beam and thus a variable field of view.[41] The 53 tomograms of T cells are randomly divided into two partitions 80% to 20%: 43 for training, and 10 for testing of the network.

The dataset for testing the accuracy of divergent cell types consisted of a total of 39 tomograms containing four different cell types: 12 Huh-7, 12 BV-2, 9 MEF, and 3 β-cells.[20] To generalize the training dataset, 6 additional tomograms containing Huh-7, BV-2, and MEF cells individually were added to the training dataset in 3 different retraining. Briefly, a total of 54 tomograms were used for the entire generalization process, which means that another 18 tomograms were used for training, and 39 were used for testing. The experimental data for training the base level of the ACSeg (as in Figure 2), that is 10 T cell SXT datasets are published on heiDATA https://doi.org/10.11588/data/XEBZLL.

METHOD DETAILS

Semi-automated labeling

To generate ground truth, testing datasets were manually segmented with Slicer3D using the segment editor tool.[42,43] Similarly, we have performed manual segmentation of 43 tomograms used for training. For training, we decided to use Biomedisa which is an open-source online

platform, to segment 3D volumes based on smart interpolation of sparsely segmented slices.[22] To generate 3D masks semi-automatically, labels were assigned manually to cell cytoplasm and polystyrene beads in every 20th slice. These sparsely labeled slices were submitted to Biomedisa for smart interpolation to obtain labels of whole 3D volume. If the generated 3D labels were mislabeled or the quality to the naked eye was insufficient, we added a few manually labeled slices. Of 43 tomograms used in this work, 95 percent were segmented with 20 ± 3 manually labeled slices, and for 5 percent of 3D tomograms 30 ± 3 slices were required to obtain 3D labels.

Model training

In this work, we applied 3D U-net integrated into the online platform Biomedisa. This implementation of the 3D U-net is one level deeper than classical 3D U-net.[44] Details on the network architecture and parameters used in the 3D U-net of Biomedisa can be found elsewhere.[22] The model was trained on 43 SXT tomograms containing a different number of T cells and polystyrene beads with the following parameters: 200 epochs, a batch size of 24, and a learning rate of 0.01. The training data were split (80%) and (20%) for training and self-validation of the network as controlled by the Biomedisa parameter settings. The best network is achieved after 33 hours. The ACSeg model is published and available online as ACSeg.h5, see "Cytoplasm" in the Biomedisa gallery https://biomedisa.info/gallery/.

QUANTIFICATION AND STATISTICAL ANALYSIS

All statistical analyses were undertaken using Python within the Visual Studio environment. Fiji[45] was employed to generate sparse labels, and subsequently, Biomedisa[22] was utilized to produce fully labeled datasets. t-test analyses were performed to determine statistical significance between the ground truth and our model files.